INORGANIC CHEMISTRY FRONTIERS

RESEARCH ARTICLE

View Article Online
View Journal | View Issue

Cite this: *Inorg. Chem. Front.*, 2023, **10**, 7369

Boosted charge transfer in Pt cluster anchored TiO_2 microspheres with rich oxygen vacancies for solar driven H_2 production from lignocellulosic biomass†

Fu-Guang Zhang,‡[a] Miao Cheng,‡[b] Yong-Jun Yuan, *[a] Qing-Yu Liu,[a] Quan Cheng[a] and Jie Guan*[c]

Solar driven lignocellulosic biomass-to-H_2 conversion through photocatalysis is an economical and clean approach to generate hydrogen fuel. However, the photocatalytic lignocellulosic biomass-to-H_2 conversion efficiency is still very low owing to the lack of a highly reactive photocatalyst. Herein, we reported the construction of Pt nanocluster chemically anchored porous TiO_2 microspheres with abundant oxygen vacancies as a highly efficient photocatalyst for solar driven lignocellulosic biomass-to-H_2 conversion. The oxygen vacancies on the TiO_2 surface not only boost electron transfer across the Pt–TiO_2 interface, but also benefit the formation of $^{\bullet}OH$ which acts as a key intermediate for the oxidation of lignocellulose. The Pt/TiO_2 photocatalysts show high photocatalytic performance with the highest H_2 generation rate of 494 μmol g^{-1} h^{-1} and an apparent quantum yield of 3.21% at 380 nm in α-cellulose aqueous solution. Furthermore, photocatalytic H_2 production from lignocellulosic biomass has been successfully achieved, and the H_2 generation rate of the optimal Pt/TiO_2 photocatalyst in rice straw, wheat straw, polar wood chip, bamboo, rice hull and corncob aqueous solution was 2, 3, 23, 32, 11 and 6 μmol g^{-1} h^{-1}, respectively. This study provides an opportunity for encouraging more research on solar driven lignocellulosic biomass-to-H_2 conversion.

Received 19th September 2023,
Accepted 28th October 2023

DOI: 10.1039/d3qi01894f

rsc.li/frontiers-inorganic

1. Introduction

Photocatalytic H_2 production from lignocellulosic biomass using solar energy to drive the reaction of lignocelluloses with water into H_2 and CO_2 over a semiconductor photocatalyst provides a "green" way to achieve the conversion of lignocellulosic biomass to H_2 fuel, which has recently attracted a lot of research attention due to its unique advantages of simplicity, low cost, *etc.*[1–8] Different from these classical enzymatic fermentation and thermocatalytic technologies,[9–11] the H_2 generated from photocatalytic systems can be easily separated and collected for utilization. Since lignocellulose has a complex and highly robust structure with staggered cellulose, hemicellulose and lignin (Fig. 1a), the oxidation and decomposition of lignocellulose are difficult kinetically. Currently, visible-responsive photocatalysts used for photocatalytic H_2 production from lignocellulose are limited to a few specific materials. For example, some studies have shown that CdO_x modified CdS (CdO_x/CdS) and cyanamide-functionalized carbon nitride (^{NCN}g-C_3N_4) photocatalysts are capable of transferring holes to lignocellulose through the cyanamide group and CdO_x acted as the hole-transfer bridge,[12,13] resulting in the oxidation of lignocellulose and H_2 production. Apart from these photocatalysts with a specific group or species, the $^{\bullet}OH$ radical with high reactivity generated by reaction of photogenerated holes in the valence band (VB) of photocatalysts with OH^- was recognized as the critical intermediate for the decomposition of lignocelluloses.[14,15] Because of the harsh thermodynamic requirements for $^{\bullet}OH$ generation, only some wide-gap semiconductors were demonstrated to be active photocatalysts for photocatalytic lignocellulosic biomass-to-H_2

[a]*College of Materials and Environmental Engineering, Hangzhou Dianzi University, Hangzhou 310018, People's Republic of China*
[b]*School of Chemistry and Chemical Engineering, Southeast University, Nanjing 211189, People's Republic of China*
[c]*School of Physics, Southeast University, Nanjing 211189, People's Republic of China. E-mail: yjyuan@hdu.edu.cn, guanjie@seu.edu.cn*

†Electronic supplementary information (ESI) available: Additional details of theoretical methods and characterization, characterization using XRD, Raman spectroscopy, N_2 adsorption–desorption curves, SEM, TEM, HADDF, spherical aberration-corrected HAADF-STEM, UV-Vis spectroscopy, and the XPS spectrum of the photocatalyst; photocatalytic H_2 production results, the light intensity of sunlight outdoors, structural models and intermediates of theoretical calculation, Mott–Schottky plots, the PL spectrum and liquid chromatography analysis and Table S1. See DOI: https://doi.org/10.1039/d3qi01894f

‡These authors contributed equally to this work.

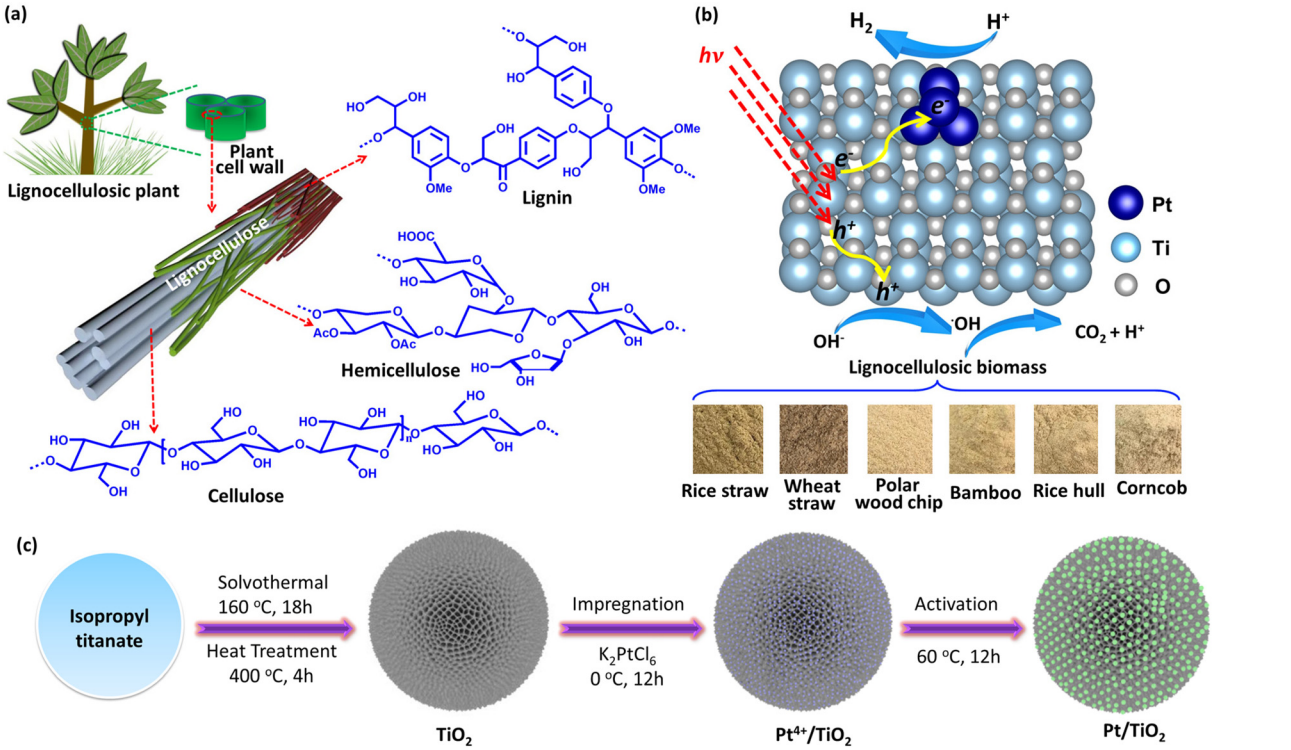

Fig. 1 (a) Chemical composition and structure of lignocellulose biomass. (b) Photocatalytic H_2 production from lignocellulose biomass over Pt nanocluster anchored porous TiO_2 microsphere photocatalysts. (c) Schematic illustration for the synthesis of Pt/TiO_2 photocatalysts.

conversion. Very recently, we reported the use of (001) facet exposed ultrathin anatase TiO_2 nanosheets as a highly active photocatalyst for photocatalytic H_2 production from lignocellulose. Owing to the low energy barrier for $^{\bullet}OH$ generation over the (001) facet and the rapid charge separation resulting from the ultrathin structure, the ultrathin TiO_2 nanosheets showed a relatively high photocatalytic H_2 production activity with a H_2 generation rate of 275 μmol h^{-1} g^{-1} and an apparent yield of 1.89% at 380 nm in the presence of Pt nanoparticles as a cocatalyst.[16] Although some progress has been made by using the (001) facet exposed ultrathin TiO_2 nanosheets as the photocatalyst, the photocatalytic H_2 production performance is still low. And thus, the development of highly efficient photocatalysts remains the biggest challenge for photocatalytic H_2 production from lignocellulosic biomass.

There are three main factors that efficiently affect the photocatalytic activity of TiO_2 for H_2 production from lignocellulose, including the active sites of the photocatalyst for $^{\bullet}OH$ generation, the active sites of the cocatalyst for H_2 generation and the carrier separation efficiency of the photocatalyst. It is highly desirable that the construction of photocatalysts with abundant active sites for both $^{\bullet}OH$ and H_2 generation reactions as well as rapid charge separation efficiency would be the most effective way to improve the photocatalytic lignocellulose-to-H_2 conversion performance of TiO_2 photocatalysts. Herein, we reported the construction of Pt nanocluster anchored porous TiO_2 microsphere (Pt/TiO_2) photocatalysts with abundant oxygen vacancies for photocatalytic lignocellulosic biomass-to-H_2 conversion (Fig. 1b). The oxygen vacancies on the TiO_2 surface benefit both the charge transfer across the Pt/TiO_2 interface and the formation of $^{\bullet}OH$ and the small size of Pt benefits the H_2 evolution reaction. As a result, the Pt/TiO_2 catalyst was demonstrated to be an efficient photocatalyst for photocatalytic H_2 production from α-cellulose as well as lignocellulosic biomass such as rice straw, wheat straw, polar wood chip, bamboo, rice hull and corncob. The highest H_2 generation rate of Pt/TiO_2 photocatalysts from α-cellulose aqueous solution was 494 μmol g^{-1} h^{-1} with an apparent quantum yield of 3.21% at 380 nm.

2. Results and discussion

2.1 Preparation and characterization

Fig. 1c shows the rapid synthetic method for Pt/TiO_2 photocatalysts. The preliminary porous TiO_2 microspheres were prepared from titanium isopropyl in acetone solution by a solvothermal method, and the preliminary product was then heated at 400 °C under air to remove the adsorbed organics. During the solvothermal process, the condensation hydrolysis of acetone results in the generation of H_2O, which provides the oxygen source for the growth of TiO_2 microspheres,[17] but TiO_2 microspheres cannot be prepared from an acetone–water solution by using H_2O as the oxygen source. To grow the Pt nanoclusters on porous TiO_2 microspheres, tetravalent Pt species was firstly bonded to porous TiO_2 microspheres by stirring the

mixed aqueous solution of TiO_2 and K_2PtCl_6 in an ice bath in a dark environment, and then the tetravalent Pt species with relatively strong oxidability was reduced to Pt on porous TiO_2 microspheres at 60 °C, resulting in the formation of a Pt nanocluster anchored TiO_2 microsphere photocatalyst (Pt/TiO_2), and the reduction of tetravalent Pt species can produce oxygen vacancies in TiO_2 in an oxygen-deficient environment.[18] The X-ray diffraction analysis in Fig. S1† confirms that the TiO_2 microspheres have a crystal structure of the anatase phase (JCPDS No. 21-1272),[19] and the heat treatment does not change the crystal phase. As for these Pt/TiO_2 samples, no diffraction peak of Pt was observed in the XRD patterns (Fig. S2†), which could be related to the low content and high dispersion of Pt on TiO_2. The N_2 adsorption–desorption curves of the as-prepared porous TiO_2 microspheres show a large Brunauer–Emmett–Teller (BET) specific surface area of 145 $m^2 g^{-1}$ (Fig. S3†) and an average porous size of 9.5 nm (inset in Fig. S3†). And then, the morphology and microstructure of bare TiO_2 and Pt/TiO_2 samples were investigated by SEM and TEM analysis. As shown in Fig. 2a and b, the as-prepared TiO_2 exhibited the typical microspherical morphology, and the average diameter of TiO_2 microspheres was estimated to be 0.87 μm (Fig. S4†). The SEM analysis showed that heat treatment does not change the morphology and size of TiO_2 (Fig. S5 and S6†), indicating that the morphology of TiO_2 was formed during the solvothermal process. The TEM image of TiO_2 microspheres illustrated in Fig. 2c shows that the surface of TiO_2 microspheres is very rough rather than smooth, confirming the porous structure of TiO_2. The rough surface is related to the existence of abundant TiO_2 nanoparticles on the surface of TiO_2 microspheres (Fig. S7†). After the growth of Pt nanoclusters, the morphology of Pt/TiO_2 microspheres does not change as compared to that of bare TiO_2 microspheres, as demonstrated by SEM and TEM analysis shown in Fig. S8 and S9.† For Pt/TiO_2 samples, the existence of Pt nanoclusters was not observed in the TEM images of the Pt/TiO_2 samples (Fig. S9 and S10†), which can be attributed to the low amount and small size of Pt nanoclusters, but the existence of Pt element can be observed in the EDX elemental mapping images of the Pt/TiO_2 samples (Fig. S11 and S12†). Spherical aberration-corrected HAADF-STEM was then used to investigate the existence of Pt on TiO_2 microspheres. As shown in

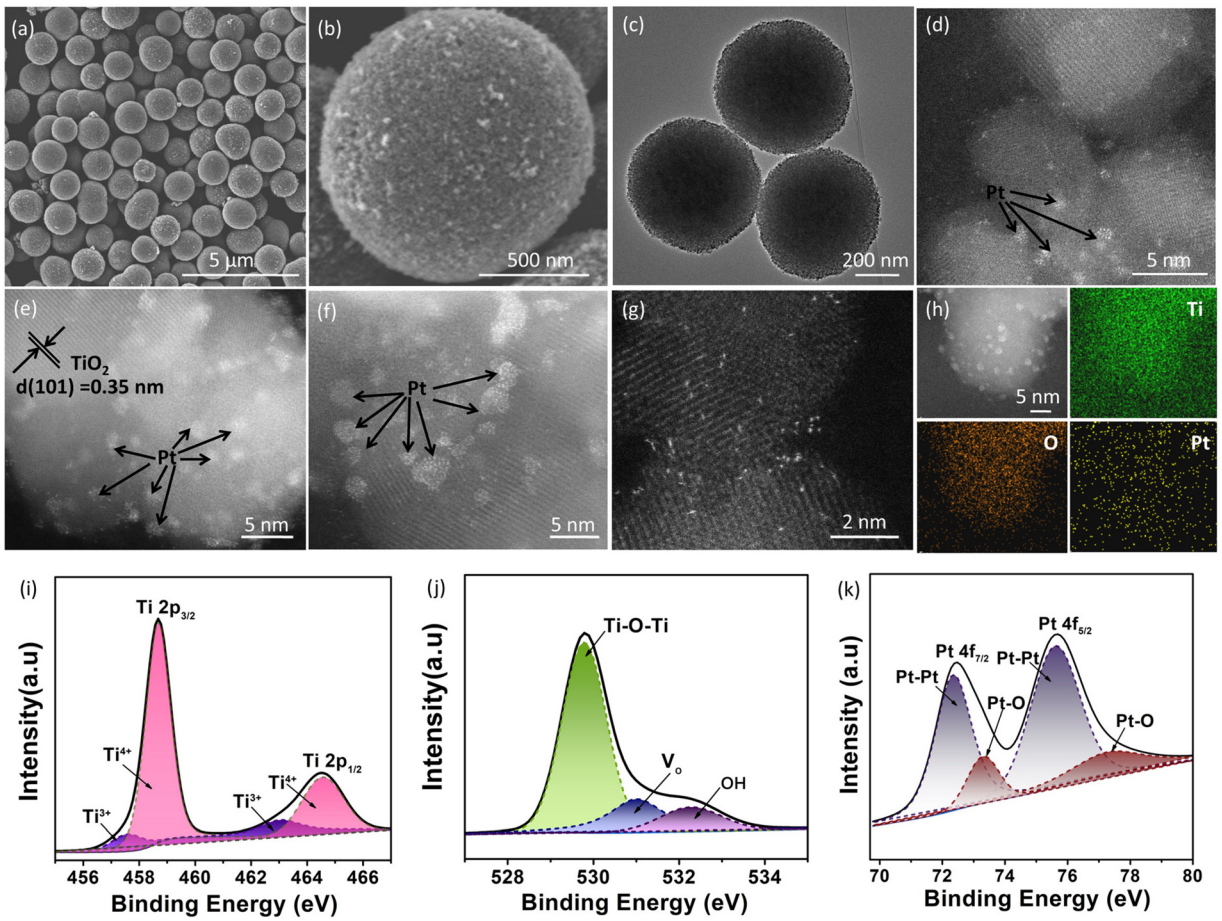

Fig. 2 (a and b) SEM and (c) TEM image of bare TiO_2. (d–g) Spherical aberration-corrected HAADF-STEM image of 0.2% Pt/TiO_2 (d), 0.4% Pt/TiO_2 (e and g) and 1.0% Pt/TiO_2 (f). (h) HAADF-STEM and elemental mapping images of 0.4% Pt/TiO_2. (i–k) High-resolution Ti 2p, O 1s and Pt 4f XPS spectra of 0.4% Pt/TiO_2.

Fig. 2d–f, obvious Pt nanoclusters can be observed in the spherical aberration-corrected HAADF-STEM images of the Pt/TiO_2 samples with an average diameter of 0.95 nm (Fig. S13†). Meanwhile, clear lattice fringes of 0.35 nm corresponding to the (101) planes of anatase TiO_2 were seen in the spherical aberration-corrected HAADF-STEM image (Fig. 2e).[20] The Pt nanoclusters without any lattice fringe were not strictly nanocrystalline, but were made up of random Pt atoms, and this relatively highly disordered structure of Pt nanoclusters is beneficial for catalyzing the H_2 evolution reaction owing to the increased number of active sites. Meanwhile, the white bright dots corresponding to the single Pt atoms were located on the surface of TiO_2 (Fig. 2g). The TEM analysis shows that the Pt species on the TiO_2 surface was mainly exhibited in the form of nanoclusters rather than single atoms, which could be attributed to the fact that the formation of Pt single atoms requires relatively harsh conditions of abundant coordination-unsaturated anions. In addition, the corresponding EDS elemental mapping images of Ti, O and Pt elements in Fig. 2h confirm the uniform distribution of Pt element in the Pt/TiO_2 photocatalyst.

The light-harvesting ability of the as-prepared bare TiO_2 and Pt/TiO_2 investigated by UV-Vis diffuse reflectance spectroscopy shows that the bare TiO_2 only shows a strong absorption peak in the UV region with an absorption edge at 397 nm (Fig. S14†). With the introduction of Pt, the Pt/TiO_2 samples exhibit a strong absorption in the UV region as well as a low weak absorption in the visible region, which is consistent with the color change from white to faint yellow. The visible light-harvesting ability of the Pt/TiO_2 samples can be referred to as an absorption tail caused by defect of oxygen vacancies as well as the light-absorption of Pt.[21,22] Although the Pt/TiO_2 samples exhibit weak visible light absorption, the bandgap of TiO_2 in the Pt/TiO_2 photocatalysts does not show an obvious red-shift as compared to that of bare TiO_2 (Fig. S14†). The electronic states of bare TiO_2 and Pt/TiO_2 photocatalysts were then investigated by X-ray photoelectron spectroscopy (XPS). The survey XPS spectrum for the 0.4% Pt/TiO_2 photocatalyst in Fig. S15† shows strong Ti 2p and O 1s peaks as well as a weak Pt 4f peak. As shown in Fig. 2i, the Ti 2p signals with binding energies at 458.7 and 464.8 eV for Ti $2p_{3/2}$ and Ti $2p_{1/2}$, respectively, were assigned to Ti^{4+}.[23] Meanwhile, a relatively weak Ti $2p_{3/2}$ and Ti $2p_{1/2}$ peak of Ti^{3+} was also observed at 457.3 and 463.1 eV, respectively.[24] That is, it is very easy to form trivalent titanium in the formation of V_O, resulting in a lower binding energy of the Ti 2p peak.[25] Furthermore, the O 1s XSP spectrum in Fig. 2j can be deconvoluted into three peaks at 529.7, 531.4 and 533.3 eV, which can be attributed to the Ti–O–Ti, V_O and surface oxygen species, respectively.[26] And a stronger peak related to Vo was observed in the O 1s XPS of the 0.4% Pt/TiO_2 sample as compared to that of bare TiO_2 (Fig. S16†), suggesting more V_O exhibited in the Pt/TiO_2 sample. As for the high-resolution Pt 4f XPS peak of 0.4% Pt/TiO_2 shown in Fig. 2k, two peaks of $4f_{7/2}$ and $4f_{5/2}$ respectively located at 72.8 and 75.9 eV can be deconvoluted into four sub peaks at 71.6, 72.9, 75.1 and 76.2 eV, in which the peaks at 71.6 and 75.1 eV can be attributed to the Pt–Pt species in Pt, and the peaks at 72.9 and 76.2 eV can be attributed to the Pt atoms bonded to the O atoms at the interface of TiO_2.[22] It is obvious that the signal peak of Pt–Pt species was much stronger than that of the Pt–O bond, confirming that Pt^0 exhibited in the form of Pt nanoclusters was the main component of Pt. And then, the existence of oxygen vacancies (V_Os) in the Pt/TiO_2 sample was confirmed by electron paramagnetic resonance (EPR) analysis. As displayed in Fig. S17,† a very weak peak with a g value at 2.003 related to V_O was observed for the bare TiO_2 sample.[27,28] After the introduction Pt on TiO_2, the EPR peak of V_O remarkably strengthens, indicating that a higher V_O concentration was present in 0.4% Pt/TiO_2 as compared to that of bare TiO_2.

2.2 The effect of Pt on H_2 generation of Pt/TiO_2 catalysts

Generally, an efficient cocatalyst used for photocatalytic H_2 production is usually an excellent H_2 generation reaction electrocatalyst, and thus the electrocatalytic performance can provide important information to identify whether it qualifies as a suitable cocatalyst.[29] From this view, the electrocatalytic H_2 generation performance of various Pt/TiO_2 catalysts was studied in 0.5 M H_2SO_4 aqueous solution using a typical three cell system. The linear sweep voltammetry (LSV) plots displayed in Fig. 3a show that bare TiO_2 is an ineffective catalyst for electrocatalytic H^+ reduction, but the introduction of Pt can promptly improve the electrocatalytic activity of TiO_2, which can be attributed to the positive effect of Pt in accelerating hydrogen release. Obviously, owing to the increasing active sites for the H_2 generation reaction, the Pt/TiO_2 catalysts display a higher electrocatalytic activity with the increased amount of Pt. Under a hold potential of −0.3 V *vs.* RHE, the current density increases quickly from 0.18 to 4.05 mA cm^{-2} when the Pt amount increases from 0 to 1.0%. Besides, only −0.38 V was required for 1.0% Pt/TiO_2 to achieve a current density of 10 mA cm^{-2}. These results suggest that Pt would be an efficient cocatalyst to enhance photocatalytic H_2 production from lignocellulosic biomass.

The photocatalytic lignocellulosic biomass-to-H_2 conversion performance of the as-prepared Pt/TiO_2 was evaluated by using α-cellulose, rice straw, wheat straw, polar wood chip, bamboo, rice hull and corncob powder as the lignocellulosic biomass in neutral aqueous solution under 300 W Xe irradiation. In view of the fact that the lignocellulosic biomass is mainly composed of cellulose, hemicelluloses and lignin, and the proportion of cellulose is the largest, cellulose was used as the lignocellulosic substrate to optimize the amount of Pt in Pt/TiO_2 for photocatalytic H_2 production. Fig. 3b compares the photocatalytic H_2 production activity of various Pt/TiO_2 photocatalysts as well as bare TiO_2 in cellulose aqueous solution. The bare TiO_2 sample shows a low photocatalytic activity with a H_2 generation rate of 48.3 μmol h^{-1} g^{-1}. It is notable that the introduction of Pt significantly enhances the photocatalytic H_2 production activity because Pt can improve the photogenerated carrier separation efficiency as well as provide abundant active sites for H_2 generation. The positive effect of Pt in improving photogenerated carrier separation efficiency was verified by

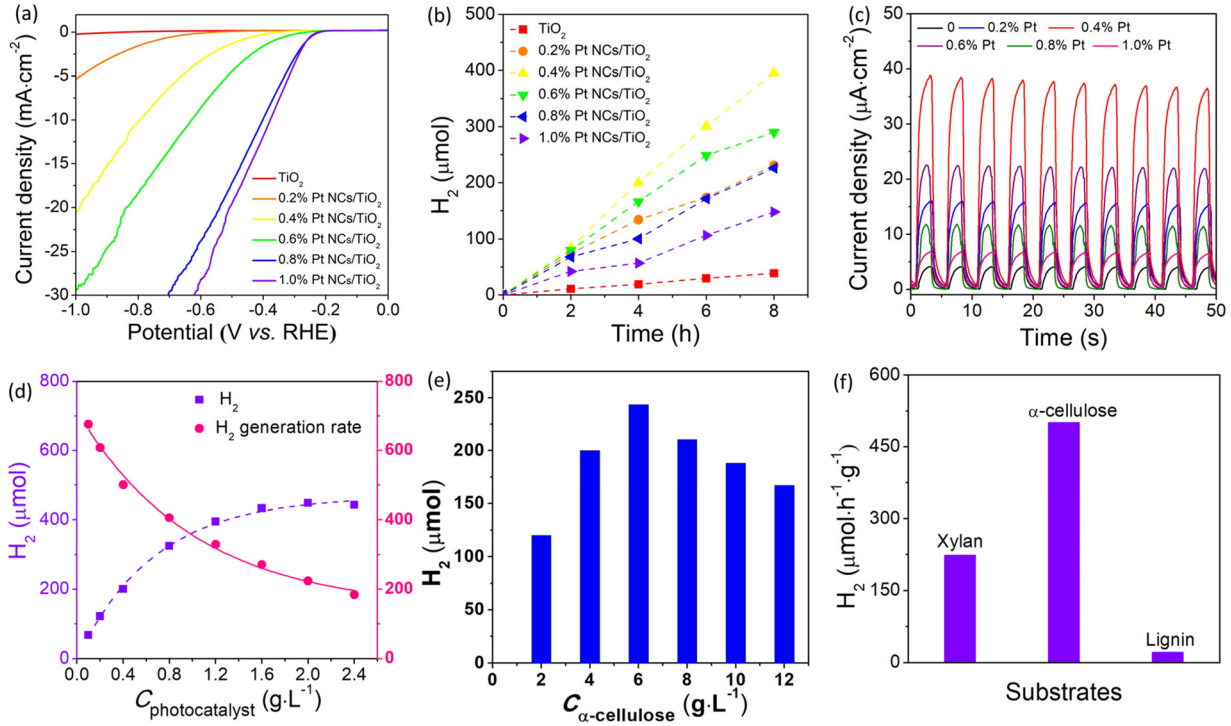

Fig. 3 (a) LSV plots of bare TiO_2 and various Pt/TiO_2 electrodes. (b) Time course of photocatalytic H_2 production over various Pt/TiO_2 photocatalysts in α-cellulose aqueous solution. (c) Photocurrent density of bare TiO_2 and various Pt/TiO_2 electrodes. (d) Photocatalytic H_2 yields as a function of photocatalyst concentration in α-cellulose aqueous solution, irradiation time 4 h. (e) Photocatalytic H_2 yields as a function of α-cellulose concentration using 0.4% Pt/TiO_2 as a photocatalyst, irradiation time 4 h. (f) Photocatalytic H_2 generation rate of 0.4% Pt/TiO_2 in α-cellulose, xylan and lignin aqueous solutions. Photocatalytic reaction conditions: 100 mg photocatalyst, 300 W Xe lamp, 1 g substrate, and 250 ml water.

transient photocurrent response measurement. Fig. 3c shows the photocurrent density of various Pt/TiO_2 electrodes modified with different amounts of Pt. The bare TiO_2 electrode shows a low photocurrent density of 4.4 μA cm^{-2}, suggesting a low carrier separation efficiency in bare TiO_2. After the introduction of Pt on TiO_2, these Pt/TiO_2 electrodes demonstrate much higher photocurrent density than that of the bare TiO_2 electrode, indicating that Pt can efficiently accelerate photogenerated carrier separation and transfer. The highest photocurrent density of 38.8 μA cm^{-2} was observed for the 0.4% Pt/TiO_2 electrode, which is about 8.8 times higher than that of the bare TiO_2 electrode. The order of photocurrent density for Pt/TiO_2 electrodes is consistent with the photocatalytic H_2 production performance of Pt/TiO_2 photocatalysts, confirming that a suitable amount of Pt plays a key factor in determining their photocatalytic activity for H_2 production. The 0.4% Pt/TiO_2 photocatalyst shows the highest H_2 generation rate of 494 μmol h^{-1} g^{-1}, which is about 10 times higher than that of bare TiO_2. The apparent quantum yield at 380 nm of this photocatalytic H_2 production system using 0.4% Pt/TiO_2 as the photocatalyst was 3.21%, which is higher than those reported for TiO_2-based photocatalysts (Table S1†). In contrast to the electrocatalytic results that the electrocatalytic activity of Pt/TiO_2 catalysts increases with the increasing amount of Pt, the further increase in the amount of Pt nanoclusters leads to a decreased photocatalytic H_2 production activity of the Pt/TiO_2 photocatalyst when the Pt amount exceeds 0.4%, which could be attributed to the aggregation of Pt as well as the shading effect of Pt.[15] The aggregation of Pt lowered the utilization efficiency of the Pt cocatalyst, while the shading effect of Pt hinders the absorption of light harvested by TiO_2. A similar phenomenon was also observed in previously reported Pt/TiO_2 systems.[30] In addition, in control experiments in the absence of any component of photocatalyst, substrate or irradiation H_2 was generated, indicating that H_2 was produced from cellulose *via* a light-catalyzed reaction. Furthermore, although the Pt/TiO_2 photocatalyst can absorb some visible light related to the formation of defect levels (V_O and Ti^{3+}) in TiO_2,[31] these Pt/TiO_2 samples were inactive photocatalysts for visible light photocatalytic H_2 production, which could be attributed to the fact that the defect level was not negative enough to reduce H^+ to H_2.[32]

2.3 The dependence of photocatalyst and substrate

To investigate the concentration dependence of the photocatalyst and substrate, photocatalytic H_2 production experiments were performed in aqueous solution with different concentrations of the photocatalyst (0.1–2.4 g L^{-1}) and substrate (2–12 g L^{-1}). As shown in Fig. 3d, the amount of H_2 evolved from the photocatalytic system with a fixed $C_{α\text{-cellulose}}$ of 4.0 g L^{-1} increases with increased $C_{photocatalyst}$. Obviously, the total amount of H_2 evolved from the photocatalytic system increases

with the increased concentration of the photocatalyst, but the H_2 generation rate decreased from 676 μmol h^{-1} g^{-1} to 184 μmol h^{-1} g^{-1} when the $C_{photocatalyst}$ changed from 0.1 g L^{-1} to 2.4 g L^{-1}, which can be attributed to the limited quantity of both illuminated photons and α-cellulose. On the other hand, at a fixed concentration of the photocatalyst (0.4 g L^{-1}), the H_2 generation rate with respect to the Pt/TiO_2 photocatalyst increases from 301 μmol h^{-1} g^{-1} at $C_{\alpha\text{-cellulose}}$ of 2 g L^{-1} to 609 μmol h^{-1} g^{-1} at $C_{\alpha\text{-cellulose}}$ of 6 g L^{-1}, and then reduces to 417 μmol h^{-1} g^{-1} at $C_{\alpha\text{-cellulose}}$ of 12 g L^{-1} (Fig. 3e). When $C_{\alpha\text{-cellulose}}$ exceeds 6 g L^{-1}, the H_2 amount decreases with the increased $C_{\alpha\text{-cellulose}}$, which is related to the shading effect of α-cellulose, that is α-cellulose as a solid substance blocks light absorbed by the photocatalyst when there is excess α-cellulose in the photocatalytic system. These results confirm that the photocatalytic H_2 production activity increases when one component was appraised with an excess of the other component.

Apart from cellulose, lignin and hemicelluloses are the other two main components of lignocelluloses, and it is very necessary to investigate the photocatalytic H_2 production performance from lignin and hemicelluloses. Because hemicellulose is a heterogeneous polymer composed of several different types of monosaccharides, and xylan is the main component of hemicelluloses, it is used instead of hemicelluloses. As shown in Fig. 3f, the photocatalytic H_2 generation activity of the 0.4% Pt/TiO_2 photocatalyst in α-cellulose, lignin and hemicelluloses (xylan from corncob) was observed to be 494, 21.2 and 765 μmol h^{-1} g^{-1}, respectively. The lowest H_2 generation rate was observed in the lignin system, which could be assigned to its more stable structure. That is, there are some glycosidic bonds in cellulose and xylan, while lignin has a polymerized aromatic group which exhibited a conjugated *para* C–C bond. It has been known that the C–C bond has a bond energy of approximately 86.2–104.3 kcal mol^{-1},[33] which is much higher than that of glycosidic bonds with a bond dissociation energy of approximately 54–72 kcal mol^{-1}.[34] And thus, lignin has higher stability and is difficult to be decomposed by the photocatalyst. It has been known that commercial TiO_2 (Degussa P25, Germany) is a highly reactive photocatalyst for H_2 production, and it is used as a reference photocatalyst. As illustrated in Fig. S18,† the photocatalytic H_2 generation rate of the 0.4% Pt/TiO_2 photocatalyst (494 μmol h^{-1} g^{-1}) was much higher than that of the 0.4% Pt/P25 sample (302 μmol h^{-1} g^{-1}), indicating that the TiO_2 microspheres are a more highly efficient photocatalyst, which could be ascribed to their large specific surface area (Fig. S3†). After the optimization of the Pt nanocluster amount, the photocatalytic H_2 production performance of 0.4% Pt/TiO_2 from lignocellulosic biomass

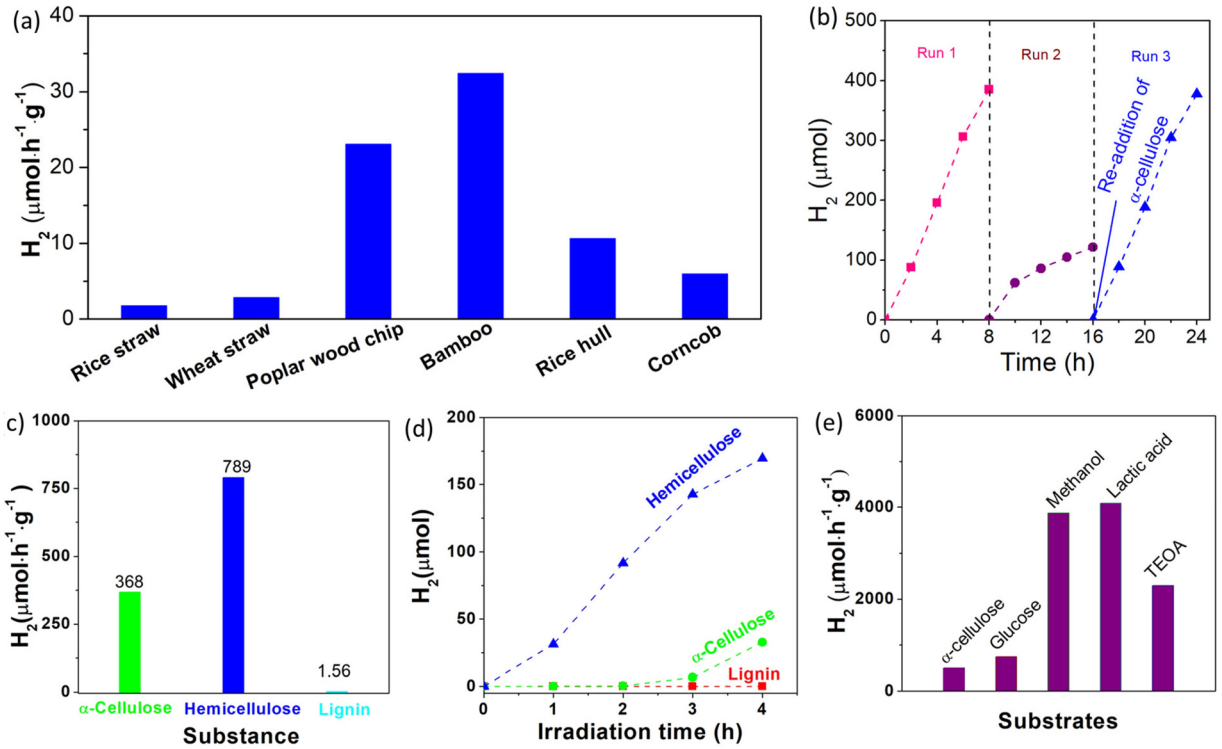

Fig. 4 (a) Photocatalytic H_2 generation rate of 0.4% Pt/TiO_2 photocatalyst from different biomass under 300 W Xe irradiation. (b) Cyclic photocatalytic H_2 production of 0.4% Pt/TiO_2 in α-cellulose aqueous solution. (c) Photocatalytic H_2 generation rate over 0.4% Pt/TiO_2 photocatalyst in α-cellulose, hemicelluloses (xylan from corncob) and lignin aqueous solutions under sunlight. (d) Time course of photocatalytic H_2 production over various 0.4% Pt/TiO_2 under simulated sunlight (100 mW cm^{-2}) irradiation. (e) Comparison of H_2 generation rate of 0.4% Pt/TiO_2 photocatalyst from α-cellulose with a commonly used electron donor under 300 W Xe irradiation. Photocatalytic reaction conditions: 100 mg photocatalyst, 1 g substrate, and 250 ml of water.

including rice straw, rice hull, corncob, wheat straw, polar wood chip and bamboo powder was investigated. As shown in Fig. 4a, the H_2 generation rate with respect to the 0.4% Pt/TiO_2 photocatalyst in rice straw, wheat straw, polar wood chip, bamboo, rice hull and corncob aqueous solution was 2, 3, 23, 32, 11 and 6 μmol h^{-1} g^{-1}, respectively. As compared to the photocatalytic H_2 production system in α-cellulose solution, the photocatalytic activity of the 0.4% Pt/TiO_2 photocatalyst was lower in these lignocellulosic biomass solutions mentioned above, which is related to the larger size of lignocellulosic biomass. Furthermore, relatively higher photocatalytic H_2 production performance was obtained for the photocatalytic system of polar wood chip and bamboo as compared to that of rice straw, rice hull, corncob, wheat straw and corncob, which could be related to the higher proportion of cellulose in their composition.

To investigate the stability of the Pt/TiO_2 photocatalyst for photocatalytic H_2 generation in a cellulose aqueous solution, the photocatalytic H_2 generation experiments were performed for 24 h with intermittent evacuation every 8 h. As shown in Fig. 4b, the H_2 generation rate does not remarkably decrease during the first run, but the amount of evolved H_2 levels off during the second run, and the average H_2 generation rate during the second run is only about 31.5% of that in the first run. The noticeable degradation of photocatalytic H_2 production performance can be assigned to the inactivation of the Pt/TiO_2 photocatalyst and/or the consumption of cellulose. To reveal the real causes for the noticeable degradation, original amount (1.0 g) of cellulose was re-added into the photocatalytic reaction solution after 16 h of irradiation. The H_2 generation rate recovers quickly during the third run after the re-addition of 1.0 g cellulose and reached 472 μmol h^{-1} g^{-1}. These results clearly reveal that the noticeable degradation of the H_2 generation rate can be due to the consumption of cellulose rather than the inactivation of the Pt/TiO_2 photocatalyst, indicating that the Pt/TiO_2 photocatalyst has high stability for photocatalytic H_2 production.

2.4 Outdoor photocatalytic testing

To obtain more insight into the photocatalytic activity of the Pt/TiO_2 photocatalyst under sunlight, photocatalytic H_2 production experiments were carried out in a sealed glass reaction flask under outdoor sunlight (Fig. S19†). As shown in Fig. 4c, H_2 gas was continuously produced in α-cellulose, hemicelluloses (xylan from corncob) and lignin aqueous solutions under direct sunlight outdoors during a 4 h test, and the H_2 generation rate was estimated to be 368, 789 and 1.56 μmol h^{-1} g^{-1}, respectively. Under simulated sunlight irradiation with a light power density of 100 mW cm^{-2}, the H_2 generation rate with respect to the 0.4% Pt/TiO_2 photocatalyst in α-cellulose, hemicelluloses (xylan from corncob) and lignin was found to 82, 424 and 0 μmol h^{-1} g^{-1}, respectively (Fig. 4d). Although the light intensity of sunlight outdoors (Fig. S20†) was weaker than that of simulated sunlight, the photocatalytic H_2 activity of the Pt/TiO_2 photocatalyst under sunlight irradiation exceeds that under simulated sunlight irradiation, which can be assigned to the large irradiation area (Fig. S21†). It has been known that glucose,[35] methanol,[36] lactic acid,[37] and triethanolamine (TEOA)[38] are frequently used as sacrificial reagents in semiconductor-based photocatalytic H_2 production systems, and they were used as references for comparison. As shown in Fig. 4e, the H_2 generation rate with respect to the 0.4% Pt/TiO_2 photocatalyst in the presence of only 1 g glucose, methanol, lactic acid and triethanolamine was respectively observed to be 740, 3867, 4085, and 2294 μmol h^{-1} g^{-1}, demonstrating the excellent photocatalytic activity of the Pt/TiO_2 photocatalysts. As compared to the photocatalytic systems in α-cellulose and lignocellulosic biomass, a higher photocatalytic H_2 production performance of the Pt/TiO_2 photocatalyst was observed in glucose, methanol, lactic acid and TEOA solution, which can be ascribed to the following reasons: one is that the α-cellulose and lignocellulosic biomass were in the solid state, in which it is difficult to react directly with solid photocatalysts owing to the absence of effective molecular collisions. The other reason is the fact that the photogenerated holes cannot directly oxidize lignocellulose but they can directly oxidize glucose, methanol, lactic acid and TEOA owing to their strong reducibility. The Pt/TiO_2 photocatalyst shows a lower photocatalytic H_2 production performance in the lignocellulose system as compared to that in methanol, lactic acid and TEOA systems under the same reaction conditions, as the oxidation and decomposition of lignocellulose are the most difficult processes, which is thus related to the modest number of surface active sites of TiO_2. Therefore, the large surface area of porous TiO_2 with abundant active sites for $^{\bullet}OH$ generation could be more important for the enhanced photocatalytic activity of Pt/TiO_2 photocatalysts for H_2 production from lignocellulose.

2.5 Effect of O vacancy

DFT calculations were performed to understand the effect of V_O on the electron transfer between Pt nanoclusters and TiO_2. The electrostatic potential distributions for the Pt nanoclusters consisting of 4 Pt atoms on the pristine TiO_2 surface (Pt/TiO_2) and the TiO_2 surface with a single V_O (Pt/V_O–TiO_2) were calculated, and the results are shown in Fig. 5a and b. It is found that as a result of the V_O right below the Pt (the position of the V_O is shown in Fig. S22†), the Pt atoms are bound to the TiO_2 surface more closely in Pt/V_O–TiO_2. The bond lengths between Pt_1, Pt_2, Pt_4 and their neighboring O atoms change from 2.19, 2.29 and 2.17 Å to 2.16, 2.06, and 2.19 Å, respectively. The generally shorter Pt–O bond lengths result in a relatively lower energy barrier for the electron transfer across the interface. For instance, the space near the middle of the Pt_2–O bond (highlighted by the red circles in the side view) is not wrapped by the isosurface with the electrostatic potential energy of 9 eV in Pt/TiO_2, indicating a transferring energy barrier higher than 9 eV for the electrons at the Fermi level. In Pt/V_O–TiO_2, the reverse happens due to the obviously shorter bond length. These results indicate that V_O defects provide a better channel for electron transfer between the TiO_2 surface and Pt nanoclusters. The differential charge density distribution for attach-

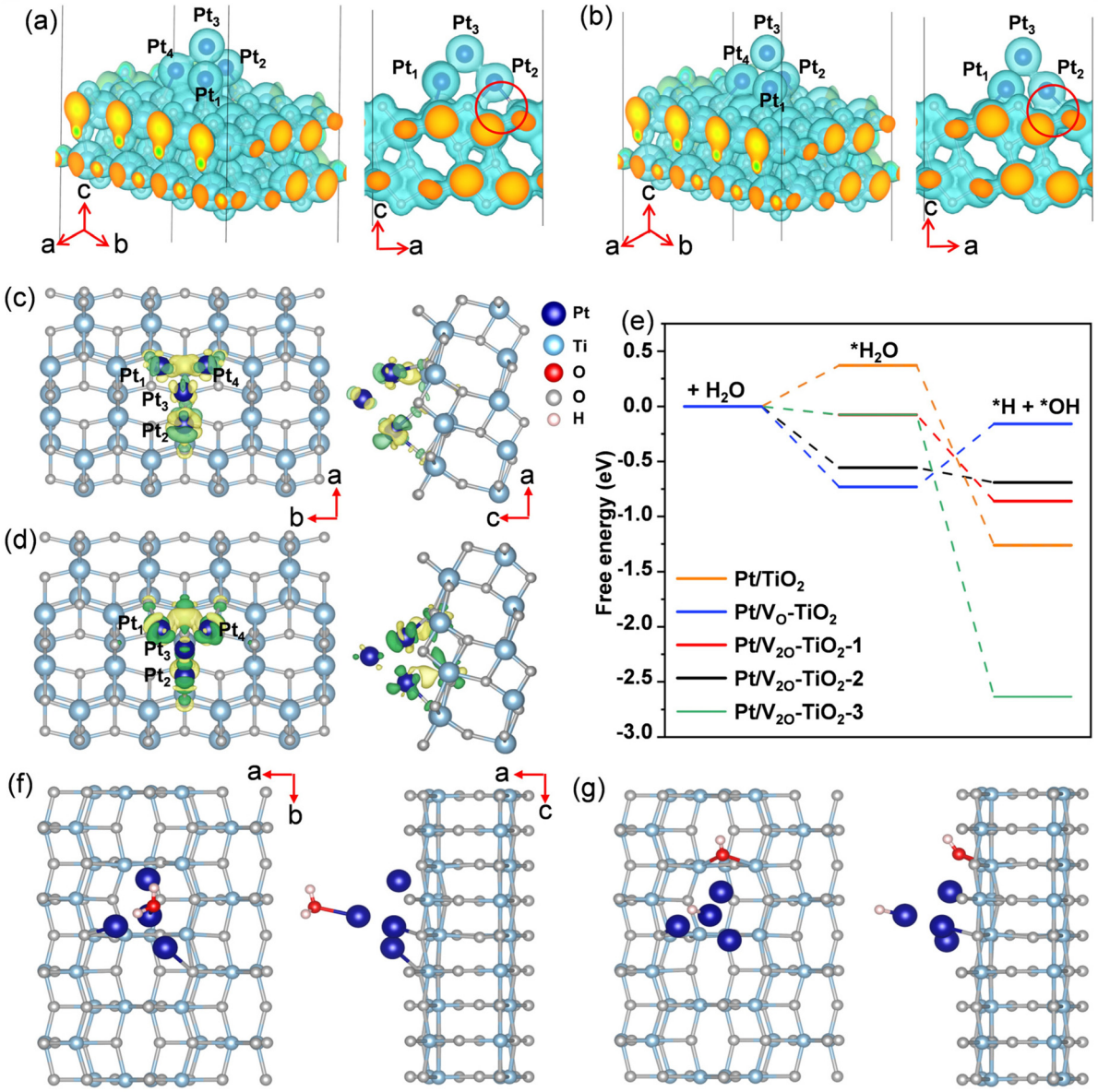

Fig. 5 (a and b) 3D spatial distribution of electrostatic potential energy for Pt/TiO_2 (a) and Pt/V_O–TiO_2 (b) in both tilted (left) and side (right) views. Electrons in the isosurface bounding regions have electrostatic potential energy lower than 9 eV, where the Fermi level is set as 0 eV. The red circles in the side view are used to highlight the differences between (a) and (b). (c and d) Calculated differential charge density of Pt/TiO_2 (c) and Pt/V_O–TiO_2 (d), where green and yellow colors of the isosurfaces represent the dissipation and accumulation of electrons. (e) Free energy profiles for the H_2O decomposition reaction on Pt/TiO_2 with no V_O, single V_O and double V_Os at different positions. (f and g) Structure for $*H_2O$ (f) and *OH/*H (g) adsorbed on the Pt/V_{2O}–TiO_2-2 surface.

ing Pt nanoclusters on the TiO_2 surface were further calculated in both Pt/TiO_2 and Pt/V_O–TiO_2, as shown in Fig. 5c and d. It can be seen that there is an obvious electron redistribution when a single V_O is involved and relatively greater electron dissipation is found in TiO_2 for Pt/V_O–TiO_2 in comparison to Pt/TiO_2. The Bader charge analysis shows that the Pt nanoclusters give 0.45 electrons to the TiO_2 surface in Pt/TiO_2 while they gain 0.13 electrons from the TiO_2 surface in Pt/V_O–TiO_2. The results indicate that O-vacancies at the interface between Pt nanoclusters and the TiO_2 surface will dramatically affect the electron distribution and lead to electron-rich Pt nanoclusters, which is favorable for the *H desorption process.

In order to study the effect of V_O on the H_2O decomposition reaction, another Vo was introduced on the TiO_2 surface at different sites besides the Pt nanoclusters and three double Vo structures were constructed, namely Pt/V_{2O}–TiO_2-1, Pt/V_{2O}–TiO_2-2, and Pt/V_{2O}–TiO_2-3. The detailed positions of the vacancies in the double O-vacancy structures are shown in Fig. S22.† As is known, the decomposition of H_2O needs two steps, including the adsorption and cleavage of H_2O mole-

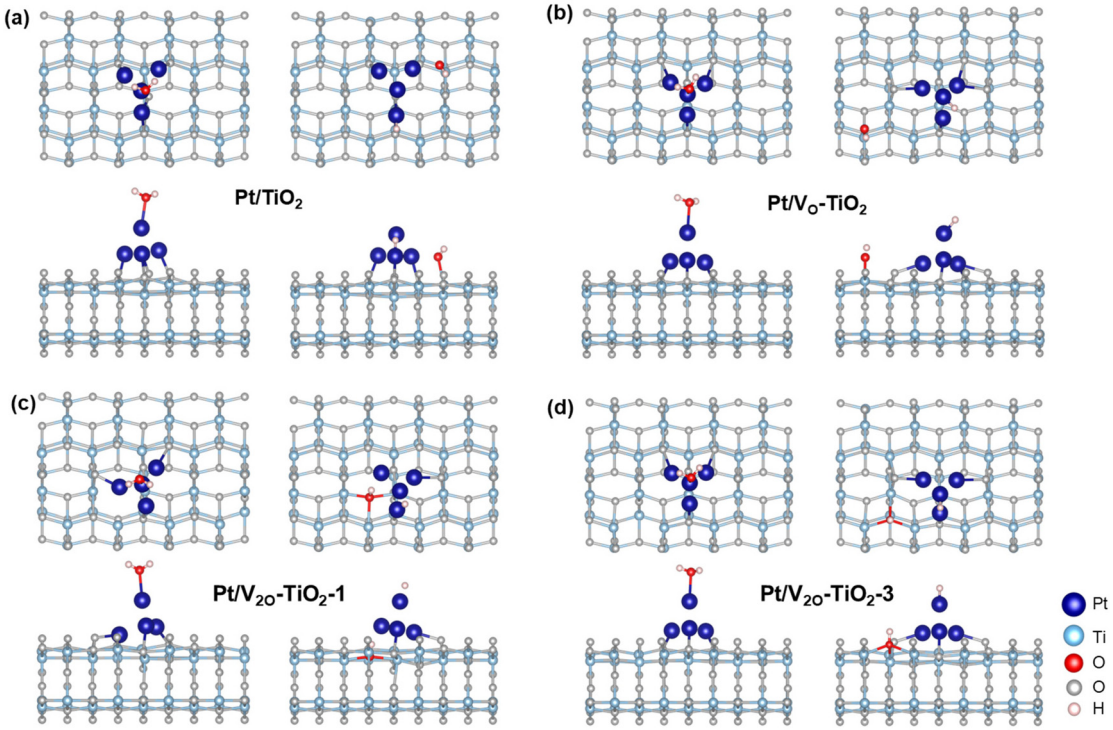

Fig. 6 Structures for *H_2O and *OH/*H adsorbed on the (a) Pt/TiO_2, (b) $Pt/V_O–TiO_2$, (c) $Pt/V_{2O}–TiO_2$-1, (d) $Pt/V_{2O}–TiO_2$-3 surfaces.

cules. As the typical geometry of the intermediates during the reaction process for $Pt/V_{2O}–TiO_2$-2 shown in Fig. 5f and g and that for the other systems shown in Fig. 6, *H_2O and *H prefer to be attached on the top of the Pt nanoclusters and *OH prefers to fill the exposed V_O. The free energy of all the intermediates for different structures was calculated and the diagram is shown in Fig. 5e. It is found that the adsorption of H_2O for all the structures with V_O is exothermic while that for Pt/TiO_2 without V_O it is endothermic. This is because the electron-rich Pt nanoclusters in the structures with V_O have an enhanced ability to transfer electrons to the electron-deficient O atom in H_2O, leading to a stronger adsorption of H_2O. In addition, when comparing the ΔG of the H_2O cleavage process for the four structures with V_O, all the structures with a double V_O exhibit an exothermic process while $Pt/V_O–TiO_2$with a single Vo exhibits an endothermic process. This is due to the dramatically larger adsorption energy of *OH filled in the Vo than that of *OH attached to a Ti atom on the pristine surface. These results show that the V_O on the TiO_2 surface benefits both the charge transfer across the Pt–TiO_2 interface and the formation of the intermediates. Finally, $Pt/V_{2O}–TiO_2$-2 is considered as the best structure for the H_2O decomposition process due to the appropriate free energy decrease during the reaction path, which will facilitate both the adsorption of H_2O and the desorption of the formed *H and *OH.

2.6 Photocatalytic mechanism exploration

To verify that Pt/TiO_2 has the ability to drive both H_2 production and lignocellulose decomposition reactions, the conduction band (CB) and valence band (VB) levels were measured by a combined method of UV-vis absorption and Mott–Schottky plot analysis.[39,40] Fig. S23† shows the Mott–Schottky plots of TiO_2 electrode with a flat band potential of approximately −0.12 V *vs.* RHE. Because the flat band potential of TiO_2 as an n-type semiconductor was generally more positive 0.2 eV than its CB level,[41]the CB level of TiO_2 was estimated to be −0.32 V *vs.* RHE, which is more negative than the reduction potential of H^+. Meanwhile, the calculated VB level of TiO_2 located at 2.80 V *vs.* RHE provides sufficient driving force for the oxidation of OH^- to $^{\bullet}OH$ [$E(^{\bullet}OH/OH^-)$ = +2.31 V *vs.* RHE],[15,42] and the generated $^{\bullet}OH$ was the critical species to oxidize lignocellulosic biomass.[43] Photoluminescence (PL) analysis utilizing terephthalic acid (TA) as a probe molecule was performed to confirm the formation of $^{\bullet}OH$ during the photocatalytic reaction since $^{\bullet}OH$ can react with TA to generate 2-hydroxyl terephthalic acid (TAOH) with a characteristic PL peak at about 430 nm, and the PL peak intensity can provide key information about the concentration of $^{\bullet}OH$.[44] Fig. S24† shows an obvious PL peak at 428 nm, confirming the successful generation of $^{\bullet}OH$ during the photocatalytic reaction. The PL peak intensity increases remarkably with increased irradiation time, indicating an increasing concentration of $^{\bullet}OH$. Furthermore, a stronger PL peak was observed for 0.4% Pt/TiO_2 as compared to that of bare TiO_2 under the same irradiation time, indicating that the introduction of Pt on TiO_2 was beneficial for $^{\bullet}OH$ generation. This phenomenon can be attributed to the positive role of Pt in improving carrier separation efficiency, which provides more holes to oxidize OH^- to generate $^{\bullet}OH$.

To obtain more insight into the oxidation and decomposition of the lignocellulosic biomass, the decomposition product after 8 h of irradiation in α-cellulose solution was analyzed by high performance liquid chromatography (HPLC). As shown in Fig. S25–S27,† mannose, ribose, glucuronic acid, glucose, xylose, arabinose, fucose and lactic acid were detected in the reaction solution, and the total organic carbon (TOC) was measured to be 0.23 mg mL^{-1}, indicating that the decomposition ratio of α-cellulose exceeds 12.9%. Furthermore, Fig. S28† shows that CO_2 was also detected in the gas of the reaction system, but the CO_2 to H_2 ratio of 7.2% is far lower than the theoretical value of 50% obtained from the equation $(C_6H_{10}O_5)_n + 7n\ H_2O = 12n\ H_2 + 6n\ CO_2$, confirming that the main oxidation products of α-cellulose were small organic molecules rather than CO_2. After the photocatalytic reaction, the residual α-cellulose was separated from the reaction solution which was characterized by FT-IR and SEM. It is obvious that residual α-cellulose exhibits surface groups of δ-C–OH, γ-CO, γ-ring, γ-C–O–C, δ-CH, δ-CH_2, γ-CH(sp_3) and γ-OH (Fig. S29†). As compared to that of fresh α-cellulose, the surface of residual α-cellulose becomes rough after the photocatalytic reaction (Fig. S30†). These results indicate that the surface of α-cellulose was constantly oxidizing during the photocatalytic reaction. Based on the above experimental observations and calculations, a proposed mechanism for the enhanced photocatalytic H_2 production from lignocellulosic biomass over Pt/TiO_2 is illustrated in Fig. S31.† When the photocatalyst was irradiated, the electrons in the VB of TiO_2 were excited to its CB, resulting in the formation of photogenerated electron–hole pairs.[45] Because the oxygen vacancies on the TiO_2 surface benefit the charge transfer across the Pt–TiO_2 interface as confirmed by DFT calculation, the photoexcited electrons in the CB of TiO_2 can rapidly transfer to Pt. The electrons accepted by Pt can reduce H^+ to evolve H_2, and the holes in the VB of TiO_2 can oxidize H_2O to $^{\bullet}OH$ promoted by oxygen vacancies on the TiO_2 surface. The $^{\bullet}OH$ radical has a strong oxidability to oxidize lignocellulose, resulting in the decomposition of lignocellulose biomass. And thus, the main reasons for the high photocatalytic performance of Pt/TiO_2 photocatalysts include the rapid charge transfer and accelerated $^{\bullet}OH$ generation rate derived from the oxygen vacancies on TiO_2 surface as well as the abundant active sites related to the large surface area of the porous TiO_2 microspheres and the small size of Pt.

3. Conclusions

In conclusion, a simple wet chemical method was developed to prepare Pt nanocluster anchored TiO_2 photocatalysts with abundant oxygen vacancies for light driven H_2 production from lignocellulosic biomass. Owing to the synergistic effect of rapid charge separation and $^{\bullet}OH$ generation promoted by oxygen vacancies as well as abundant active sites for H_2 generation, the Pt/TiO_2 photocatalysts show excellent photocatalytic performance for H_2 production from lignocellulosic biomass. The optimized Pt/TiO_2 photocatalyst shows a H_2 generation rate of 494 μmol h^{-1} g^{-1} under 300 W Xe irradiation and an apparent yield of 3.21% at 380 nm in α-cellulose aqueous solution. Meanwhile, H_2 gas was successfully evolved from lignocellulosic biomass of rice straw, rice hull, corncob, wheat straw, polar wood chip and bamboo.

Author contributions

Y. J. Yuan and J. Guan designed the experiment and co-wrote the manuscript. F. G. Zhang and Q. Y. Liu performed the preparation and characterization experiments, F. G. Zhang and Q. Cheng performed the electrochemical experiments, F. G. Zhang performed the photocatalytic H_2 production experiments, M. Cheng and J. Guan performed the theoretical calculation. All authors analyzed the data and commented on the manuscript.

Conflicts of interest

The authors declare no competing interests.

Acknowledgements

This work was supported by the Fundamental Research Funds for the Provincial Universities of Zhejiang under Grant No. GK239909299001-002, the Natural Science Foundation of Zhejiang Province under Grant No. LY21B030001, and the National Natural Science Foundation of China under Grant No. 62274028 and 22372052.

References

1 N. Luo, T. Montini, J. Zhang, P. Fornasiero, E. Fonda, T. Hou, W. Nie, J. Lu, J. Liu, M. Heggen, L. Lin, C. Ma, M. Wang, F. Fan, S. Jin and F. Wang, Visible-Light-Driven Coproduction of Diesel Precursors and Hydrogen From Lignocellulose-Derived Methylfurans, *Nat. Energy*, 2019, **4**, 575–584.

2 M. F. Kuehnel and E. Reisner, Solar Hydrogen Generation From Lignocellulose, *Angew. Chem., Int. Ed.*, 2018, **57**, 3290–3296.

3 T. Kawai and T. Sakata, Conversion of Carbohydrate into Hydrogen Fuel by a Photocatalytic Process, *Nature*, 1980, **286**, 474–476.

4 E. Lam and E. Reisner, A TiO_2-Co (terpyridine)$_2$ Photocatalyst for the Selective Oxidation of Cellulose to Formate Coupled to the Reduction of CO_2 to Syngas, *Angew. Chem., Int. Ed.*, 2021, **60**, 23306–23312.

5 V. C. Nguyen, D. B. Nimbalkar, L. D. Nam, Y. L. Lee and H. Teng, Photocatalytic Cellulose Reforming for H_2 and Formate Production by Using Graphene Oxide-Dot Catalysts, *ACS Catal.*, 2021, **11**, 4955–4967.

6 E. Wang, A. Mahmood, S.-G. Chen, W. Sun, T. Muhmood, X. Yang and Z. Chen, Solar-Driven Photocatalytic Reforming of Lignocellulose into H_2 and Value-Added Biochemicals, *ACS Catal.*, 2022, **12**, 11206–11215.

7 X. Wu, S. Xie, H. Zhang, Q. Zhang, B. F. Sels and Y. Wang, Metal Sulfide Photocatalysts for Lignocellulose Valorization, *Adv. Mater.*, 2021, **33**, 2007129.

8 C. Rao, M. Xie, S. Liu, R. Chen, H. Su, L. Zhou, Y. Pang, H. Lou and X. Qiu, Visible Light-Driven Reforming of Lignocellulose into H_2 by Intrinsic Monolayer Carbon Nitride, *ACS Appl. Mater. Interfaces*, 2021, **13**, 44243–44253.

9 Z. Sun, G. Bottari, A. Afanasenko, M. C. A. Stuart, P. J. Deuss, B. Fridrich and K. Barta, Complete Lignocellulose Conversion with Integrated Catalyst Recycling Yielding Valuable Aromatics And Fuels, *Nat. Catal.*, 2018, **1**, 82–92.

10 S. M. Shaheed, J. P. Rohit, R. Madhan and K. Selvakumar, A Comparative Study on the Production of Ethanol from Lignocellulosic Biomass by Chemical and Biological Method, *Nat. Precedings*, 2011, **6**, 1.

11 L. R. Lynd, G. T. Beckham, A. M. Guss, L. N. Jayakody, E. M. Karp, C. Maranas, R. L. McCormick, D. Amador-Noguez, Y. J. Bomble, B. H. Davison, C. Foster, M. E. Himmel, E. K. Holwerda, M. S. Laser, C. Y. Ng, D. G. Olson, Y. Román-Leshkov, C. T. Trinh, G. A. Tuskan, V. Upadhayay, D. R. Vardon, L. Wang and C. E. Wyman, Toward Low-cost Biological and Hybrid Biological/Catalytic Conversion of Cellulosic Biomass to Fuels, *Energy Environ. Sci.*, 2022, **15**, 938–990.

12 D. W. Wakerley, M. F. Kuehnel, K. L. Orchard, K. H. Ly, T. T. Rosser and E. Reisner, Solar-Driven Reforming of Lignocellulose to H_2 with a CdS/CdO_x Photocatalyst, *Nat. Energy*, 2017, **2**, 1–9.

13 H. Kasap, S. Achilleos and A. Huang, E. Photoreforming, of Lignocellulose into H_2 Using Nanoengineered Carbon Nitride under Benign Conditions, *J. Am. Chem. Soc.*, 2018, **140**, 11604–11607.

14 Q. Y. Liu, H. D. Wang, Y. J. Yuan, R. Tang, L. Bao, Z. Ma, J. Zhong, Z. T. Yu and Z. G. Zou, Visible-Light-Responsive Z-scheme System for Photocatalytic Lignocellulose-to-H_2 Conversion, *Chem. Commun.*, 2021, **57**, 9898–9901.

15 P. Wang, Y. J. Yuan, Q. Y. Liu, Q. Cheng, Z. K. Shen, Z. T. Yu and Z. G. Zou, Solar-Driven Lignocellulose-to-H_2 Conversion in Water Using 2D-2D MoS_2/TiO_2 Photocatalysts, *ChemSusChem*, 2021, **14**, 2860–2865.

16 Q. Cheng, Y. J. Yuan, R. Tang, Q. Y. Liu, L. Bao, P. Wang, J. S. Zhong, Z. Y. Zhao, Z. T. Yu and Z. G. Zou, Rapid Hydroxyl Radical Generation on (001)-Facet-Exposed Ultrathin Anatase TiO_2 Nanosheets for Enhanced Photocatalytic Lignocellulose-to-H_2 Conversion, *ACS Catal.*, 2022, **12**, 2118–2125.

17 H. Y. Wang, J. Chen, S. Hy, L. Yu, Z. Xu and B. Liu, High-Surface-Area Mesoporous TiO_2 Microspheres via One-step Nanoparticle Self-assembly for Enhanced Lithium-Ion Storage, *Nanoscale*, 2014, **6**, 14926–14931.

18 Z. W. Wei, H. J. Wang, C. Zhang, K. Xu, X. L. Lu and T. B. Lu, Reversed Charge Transfer and Enhanced Hydrogen Spillover in Platinum Nanoclusters Anchored on Titanium Oxide with Rich Oxygen Vacancies Boost Hydrogen Evolution Reaction, *Angew. Chem., Int. Ed.*, 2021, **60**, 16622–16627.

19 J. Yu, J. Low, W. Xiao, P. Zhou and M. Enhanced, Photocatalytic CO_2-Reduction Activity of Anatase TiO_2 by Coexposed {001} and {101} Facets, *J. Am. Chem. Soc.*, 2014, **136**, 8839–8842.

20 R. Song, H. Chi, Q. Ma, D. Li, X. Wang, W. Gao, H. Wang, X. Wang, Z. Li and C. Li, Highly Efficient Degradation of Persistent Pollutants with 3D Nanocone TiO_2-Based Photoelectrocatalysis, *J. Am. Chem. Soc.*, 2021, **143**, 13664–13674.

21 P. N. Duchesne and P. Zhang, Local Structure of Fluorescent Platinum Nanoclusters, *Nanoscale*, 2012, **4**, 4199–4205.

22 L. Li, J. Yan, T. Wang, Z. J. Zhao, J. Zhang, J. Gong and N. Guan, Sub-10 nm Rutile Titanium Dioxide Nanoparticles for Efficient Visible-Light-Driven Photocatalytic Hydrogen Production, *Nat. Commun.*, 2015, **6**, 5881.

23 Y. Jiang, W. Zhao, S. Li, S. Wang, Y. Fan, F. Wang, X. Qiu, Y. Zhu, Y. Zhang, C. Long and Z. Tang, Elevating Photooxidation of Methane to Formaldehyde via TiO_2 Crystal Phase Engineering, *J. Am. Chem. Soc.*, 2022, **144**, 15977–15987.

24 Y. Wang, X. Xue, P. Liu, C. Wang, X. Yi, Y. Hu, L. Ma, G. Zhu, R. Chen, T. Chen, J. Ma, J. Liu and Z. Jin, Atomic Substitution Enabled Synthesis of Vacancy-rich Two-dimensional Black TiO_{2-x} Nanoflakes for High-Performance Rechargeable Magnesium Batteries, *ACS Nano*, 2018, **12**, 12492–12502.

25 Y. Zhao, Y. Zhao, R. Shi, B. Wang, G. I. Waterhouse, L. Z. Wu, C. H. Tung and T. Zhang, Tuning Oxygen Vacancies in Ultrathin TiO_2 Nanosheets to Boost Photocatalytic Nitrogen Fixation up to 700 nm, *Adv. Mater.*, 2019, **31**, 1806482.

26 Y. Zhang, Z. Xu, G. Li, X. Huang, W. Hao and Y. Bi, Direct Observation of Oxygen Vacancy Self-Healing on TiO_2 Photocatalysts for Solar Water Splitting, *Angew. Chem., Int. Ed.*, 2019, **58**, 14229–14233.

27 Y. Bo, H. Wang, Y. Lin, T. Yang, R. Ye, Y. Li, C. Hu, P. Du, Y. Hu, Z. Liu, R. Long, C. Gao, B. Ye, L. Song, X. Wu and Y. Xiong, Altering Hydrogenation Pathways in Photocatalytic Nitrogen Fixation by Tuning Local Electronic Structure of Oxygen Vacancy with Dopant, *Angew. Chem., Int. Ed.*, 2021, **60**, 16085–16092.

28 P. A. Osorio-Vargas, C. Pulgarin, A. Sienkiewicz, L. R. Pizzio, M. N. Blanco, R. A. Torres-Palma, C. Pétrier and J. A. Rengifo-Herrera, Low-Frequency Ultrasound Induces Oxygen Vacancies Formation and Visible Light Absorption in TiO_2 P-25 Nanoparticles, *Ultrason. Sonochem.*, 2012, **19**, 383–386.

29 J. Yang, D. Wang, H. Han and C. A. N. Li, Roles of Cocatalysts in Photocatalysis and Photoelectrocatalysis, *Acc. Chem. Res.*, 2013, **46**, 1900–1909.
30 J. Yu, L. Qi and M. Jaroniec, Hydrogen Production by Photocatalytic Water Splitting Over Pt/TiO_2 Nanosheets with Exposed (001) Facets, *J. Phys. Chem. C*, 2010, **114**, 13118–13125.
31 L. Li, J. Yan, T. Wang, Z. J. Zhao, J. Zhang, J. Gong and N. Guan, Sub-10 nm Rutile Titanium Dioxide Nanoparticles for Efficient Visible-Light-Driven Photocatalytic Hydrogen Production, *Nat. Commun.*, 2015, **6**, 5881.
32 D. Ariyanti, S. Mukhtar, N. Ahmed, Z. Liu, J. Dong and W. Gao, Surface Modification of TiO_2 for Visible Light Photocatalysis: Experimental and Theoretical Calculations of its Electronic and Optical Properties, *Int. J. Mod. Phys. B*, 2020, **34**, 2040067.
33 K. Exner and P. V. R. Schleyer, Theoretical Bond Energies: a Critical Evaluation, *J. Phys. Chem.*, 2001, **105**, 3407–3416; X. Zheng, X. Wang, J. Liu, X. Fu, Y. Yang, H. Han, Y. Fan, S. Zhang, S. Meng and S. Chen, Construction of NiP_x/MoS_2/NiS/CdS Composite to Promote Photocatalytic H_2 Production from Glucose Solution, *J. Am. Ceram. Soc.*, 2021, **104**, 5307–5316.
34 X. Wu, X. Fan, S. Xie, J. Lin, J. Cheng, Q. Zhang, L. Chen and Y. Wang, Solar Energy-Driven Lignin-first Approach to Full Utilization of Lignocellulosic Biomass under Mild Conditions, *Nat. Catal.*, 2018, **1**, 772–780.
35 X. H. Zhang, M. Yang, J. G. Zhao and L. J. Guo, Photocatalytic Hydrogen Evolution with Simultaneous Degradation of Organics over $(CuIn)_{0.2}Zn_{1.6}S_2$ Solid Solution, *Int. J. Hydrogen Energy*, 2013, **38**, 15985–15991.
36 F. Guzman, S. S. C. Chuang and C. Yang, Role of Methanol Sacrificing Reagent in the Photocatalytic Evolution of Hydrogen, *Ind. Eng. Chem. Res.*, 2013, **52**, 61–65.
37 H. B. Huang, K. Yu, J. T. Wang, J. R. Zhou, H. F. Li, J. Lü and R. Cao, Controlled Growth of ZnS/ZnO Heterojunctionson Porous Bomass Carbons via One-step-carbothermal Reduction Enables Visible-Light Driven Photocatalytic H_2 Production, *Inorg. Chem. Front.*, 2019, **6**, 2035–2042.
38 C. Cheng, L. H. Mao, X. Kang, C. L. Dong, Y. C. Huang, S. H. Shen, J. W. Shi and L. J. Guo, A High-cyano Groups-Content Amorphous-Crystalline Carbon Nitride Isotype Heterojunction Photocatalyst for High-Quantum-Yield H_2 Production and Enhanced CO_2 Reduction, *Appl. Catal., B*, 2023, **331**, 122733.
39 K. Chang, M. Li, T. Wang, S. Ouyang, P. Li, L. Liu, J. Ye and J. Drastic, Layer-number-Dependent Activity Enhancement in Photocatalytic H_2 Evolution over nMoS_2/CdS ($n \geq 1$) Under Visible Light, *Adv. Energy Mater.*, 2015, **5**, 1402279.
40 P. Chen, B. Lei, X. A. Dong, H. Wang, J. Sheng, W. Cui, J. Li, Y. Sun, Z. Wang and F. Dong, Rare-Earth Single-Atom La-N Charge-Transfer Bridge on Carbon Nitride for Highly Efficient and Selective Photocatalytic CO_2 Reduction, *ACS Nano*, 2020, **14**, 15841–15852.
41 Y. J. Yuan, N. Lu, L. Bao, R. Tang, F. G. Zhang, J. Guan, H. D. Wang, Q. Y. Liu, Q. Cheng, Z. T. Yu and Z. Zou, A Metal-Free Two-Dimensional Photocatalyst for Visible-Light Photocatalytic H_2 Production and Nitrogen Fixation, *ACS Nano*, 2022, **16**, 12174–12184.
42 G. Liu, P. Niu, L. Yin and H. M. Cheng, α-Sulfur Crystals as a Visible-Light-Active Photocatalyst, *J. Am. Chem. Soc.*, 2012, **134**, 9070–9073.
43 A. Caravaca, W. Jones, C. Hardacre and M. Bowker, H_2 Production by the Photocatalytic Reforming of Cellulose and Raw Biomass using Ni, Pd, Pt and Au on Titania, *Proc. R. Soc. A*, 2016, **472**, 20160054.
44 Y. Guo, J. Li, Y. Yuan, L. Li, M. Zhang, C. Zhou and Z. Lin, A Rapid Microwave-Assisted Thermolysis Route to highly Crystalline Carbon Nitrides for Efficient Hydrogen Generation, *Angew. Chem., Int. Ed.*, 2016, **55**, 14693–14697.
45 S. Rej, S. M. H. Hejazi, Z. Badura, G. Zoppellaro, S. Kalytchuk, Š. Kment, P. Fornasiero and A. Naldoni, Light-Induced Defect Formation and Pt Single Atoms Synergistically Boost Photocatalytic H_2 Production in 2D TiO_2-Bronze Nanosheets, *ACS Sustainable Chem. Eng.*, 2022, **10**, 17286–17296.

